nature communications

Article

https://doi.org/10.1038/s41467-025-57624-w

Enantioselective synthesis of chiroplasmonic helicoidal nanoparticles by nanoconfinement in chiral dielectric shells

Received: 15 January 2025

Accepted: 24 February 2025

Published online: 11 March 2025

Check for updates

Xiaoxi Luan[1,2], Yu Tian[1], Fengxia Wu[1], Lu Cheng[3], Minghua Tang[4], Xiali Lv[1,2], Haili Wei[1,2], Xiaodan Wang[1], Fenghua Li[1], Guobao Xu[1,2] & Wenxin Niu[1,2]

Helicoid metal nanoparticles with intrinsic chirality have unveiled tailorable properties and unlocked many chirality-related applications across various fields. Nevertheless, the existing strategies for enantioselective synthesis of helicoid metal nanoparticles have been predominantly limited to gold. Here, we demonstrate a robust and versatile strategy for the enantioselective synthesis of helicoid nanoparticles beyond gold, leveraging chiral nanoconfinement provided by chiral SiO_2 or nanoshells. The chiral nanoconfinement strategy enables the decoupling of ligand-directed crystal growth from chiral induction, allowing for the independent tuning of these two critical aspects. As a result, this approach can not only facilitate the replication of chiral shapes from the chiral nanoshells but also allow the generation of alternative chiral shapes. By employing this approach, we demonstrate the enantioselective synthesis of helicoid Pt, Au@Pt, Au@Pd, Au@Ag, and Au@Cu nanoparticles. The chiroplasmonic properties of Pt- and Pd-based chiral nanoparticles have been discovered, and the inversion of chiroplasmonic properties of Ag-based chiral nanoparticles via facet control has been documented and theoretically explained. The chiral nanoconfinement strategy enriches the toolbox for creating chiral nanoparticles and supports their exploration in diverse applications.

Chirality, the property of asymmetry in an object or molecule resulting in the existence of two non-superimposable mirror image forms, is a fundamental concept observed across various disciplines, from chemistry and biology to physics and materials science[1–4]. In recent years, the manifest of chirality in inorganic nanomaterials has led to the emergence of a class of chiral materials with tailorable properties[5,6]. Unlike their organic counterparts, chiral inorganic nanomaterials not only span a diverse range of compositions, including metals[7–9], metal oxides[10,11], semiconductors[12,13], and others[14,15], but also exhibit the potential for multilevel hierarchical architectures with chiral features at various length scales[16–20]. Over the past decades, the development of nanoscience has empowered the deliberate manipulation of the size, shape, and structure of chiral inorganic nanomaterials, allowing for precise control over their chiral properties[7,21,22]. By engineering the chirality at the nanoscale, chiral inorganic nanomaterials have now found application in nanophotonics[23,24], metamaterials[25,26], plasmonics[27,28], enantioselective catalysis[29–31] and sensing[32,33], biological response[34,35]. These properties and applications further stress the need

[1]State Key Laboratory of Electroanalytical Chemistry, Changchun Institute of Applied Chemistry, Chinese Academy of Sciences, Changchun, China. [2]School of Applied Chemistry and Engineering, University of Science and Technology of China, Hefei, China. [3]National Engineering Research Center for Synthesis of Novel Rubber and Plastic Materials, Yanshan Branch of Beijing Research Institute of Chemical Industry, SINOPEC, Beijing, China. [4]Analysis and Testing Center, Soochow University, Suzhou, China. e-mail: niuwx@ciac.ac.cn

to develop strategies for the enantioselective synthesis of chiral inorganic nanoparticles (NPs) with tailored shapes and structures.

Although enantioselective synthesis is well established in modern organic chemistry, it is challenging in chiral inorganic materials such as metals[36]. Unlike organic molecules that predominantly rely on directional covalent bonds for their construction, the non-directional nature of metallic bonds poses a challenge in achieving precise chiral arrangements within metal nanomaterials. Consequently, the enantioselective synthesis of chiral metal nanomaterials is exceptionally intricate[37,38]. Furthermore, the inherent close-packed arrangements in metals often yield symmetrical structures, making the attainment of enantioselectivity challenging as it requires disrupting the inherent symmetry[39]. Despite these obstacles, innovative approaches involving chiral biomolecules[7,22,40,41], chiral micelles[9], and circular polarized light[42,43] have been harnessed to facilitate the creation of chiral metallic NPs. A significant recent advance has been the amino-acid/peptide-directed synthesis of chiral gold NPs characterized by helicoid morphologies[7]. This method effectively imparts molecular chirality to gold nanocrystals through the enantioselective interactions of L- or D-amino acids with R- or S-{*hkl*} intrinsically chiral Au surfaces. This process gives rise to the asymmetrical evolution of gold NPs and the formation of helicoid morphologies featuring highly twisted chiral structures.

The synthesis of helicoid gold NPs has unveiled their tailorable chiroplasmonic properties and unlocked many chirality-related applications such as metamaterials[44], enantiomer-dependent immunological response[16], and chiroplasmonic sensing or catalysis[45–47]. With the success of gold helicoid NPs, it is of fundamental interest that helicoid of other metals could be synthesized. Nonetheless, the amino-acid/peptide-directed synthesis method's adaptability to other metals is highly constrained[37]. The pursuit of a comprehensive and versatile strategy for generating chiral metal NPs remains a compelling goal. Here, we demonstrate a versatile strategy to synthesize chiral metallic helicoid NPs beyond gold. In this strategy, chiral silica nanoshells are leveraged as chiral transfer medium to impart their chirality onto other metal helicoid NPs (Fig. 1). Mechanistic analysis of these growth pathways highlight the importance of decoupling ligand-mediated crystal growth from chiral induction, making this strategy a general strategy for the enantioselective synthesis of helicoid Pt, Au@Pt, Au@Pd, Au@Ag NPs with replicated or alternative chiral shapes. Among these helicoid NPs, the chiroplasmonic properties of Pd- and Pt-based chiral NPs have been discovered, and the inversed chiroplasmonic properties of Ag-based chiral NPs have been achieved.

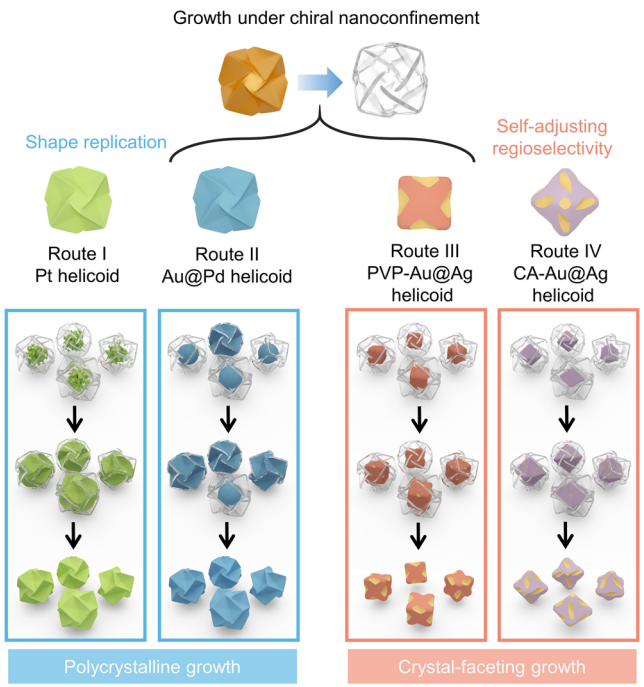

Fig. 1 | Schematic representation for the growth mechanisms of various helicoid NPs under chiral nanoconfinement. The chiral nanoconfinement strategy involves two distinct growth pathways: the shape-replicating pathway (blue) and the self-adjusting regioselective pathway (red). Depending on difference growth processes, helicoid Pt (green models) and Au@Pd NPs (blue models), which undergo polycrystalline growth and adhere to the shape-replicating pathway, follow Route I and Route II, respectively. Ag-based NPs undergo the self-adjusting regioselective pathway with faceted single-crystalline growth, which are subdivided into two routes with different crystal facets. When PVP serves as the stabilizer to promote the Ag {100} facets, helicoid Au@Ag NPs with a cubic profile (red models) follow the Route III. When CA is used as the stabilizer to promote the Ag {111} facets, helicoid Au@Ag NPs with an octahedral profile (purple models) follow the Route IV. The golden and translucent models represent the helicoid Au NPs and chiral SiO_2 nanoshells, respectively.

Results

Principles of enantioselective growth by nanoconfinement

The limitation of the existing synthetic strategy for helicoid metal NPs stems from the symmetry-breaking process, where the chiral induction process is tightly coupled with the growth process[7,17]. Both processes are significantly influenced by the strong interactions of thiolate chiral ligands with gold surfaces. Consequently, when attempting to apply the same strategy using different metals, surfactants, or chiral ligands, altering the interaction strength of ligands or the growth kinetics of NPs renders the strategy ineffective[37]. Recognizing this limitation, we hypothesize that by decoupling the chiral induction from ligand-mediated growth processes, we could establish a general and versatile strategy for synthesizing helicoid metal NPs. Inspired by the methods reported by Yin's group[48–50] and others[51,52], we propose the use of a nanoreactor technique[53,54], which can be easily generalized for the preparation of various nanomaterials. This approach does not rely on the strict control over reaction kinetics or highly material-specific ligand adsorption processes to govern nanoparticle architectures[55,56].

Based on this hypothesis, we propose a strategy for the synthesis of chiral metallic helicoid NPs other than gold. The synthesis mechanism is depicted in Figs. 1 and 2a, encompassing the following procedures: (1) the synthesis of porous chiral silica nanoshells; (2) the formation of seeds confined in chiral silica nanoshells; (3) the enantioselective growth of metals in the nanoshells, resulting in the synthesis of helicoid metal@SiO_2 NPs; (4) the removal of silica nanoshells. In this strategy, chiral silica nanoshells, completely duplicating the complex chiral structures of helicoid Au NPs, serve as the chiral transfer medium, imparting their chirality onto other metallic helicoid NPs. The chiral induction in the proposed strategy solely employs the rigid L- or D-chiral silica nanoshells, which impose physical steric hindrance for the enantioselective growth of metal helicoid NPs rather than relying on chemical adsorption of ligands[7,27] or soft supramolecular templates[9,57]. Consequently, this design effectively decouples chiral induction from ligand-mediated growth processes. By decoupling these processes, this strategy can be generalized for the enantioselective synthesis of various helicoid metal NPs, enabling the replication of chiral shapes of the SiO_2 nanoshells, or even the formation of alternative chiral morphologies (Fig. 1).

Synthesis of porous chiral SiO_2 nanoshells

To achieve the restricted growth of different metals under chiral nanoconfinement, semipermeable chiral SiO_2 nanoshells with robust rigidity, well-developed porosity, removability, and distinctive helicoid morphologies are synthesized with helicoid Au NPs as templates (Fig. 2a–g). The helicoid Au NPs are synthesized using cysteine (Cys) as chiral inducers (see Methods for details), featured with mirror-symmetric helicoid morphologies consisting of eight twisted trigonal

https://doi.org/10.1038/s41467-025-57624-w

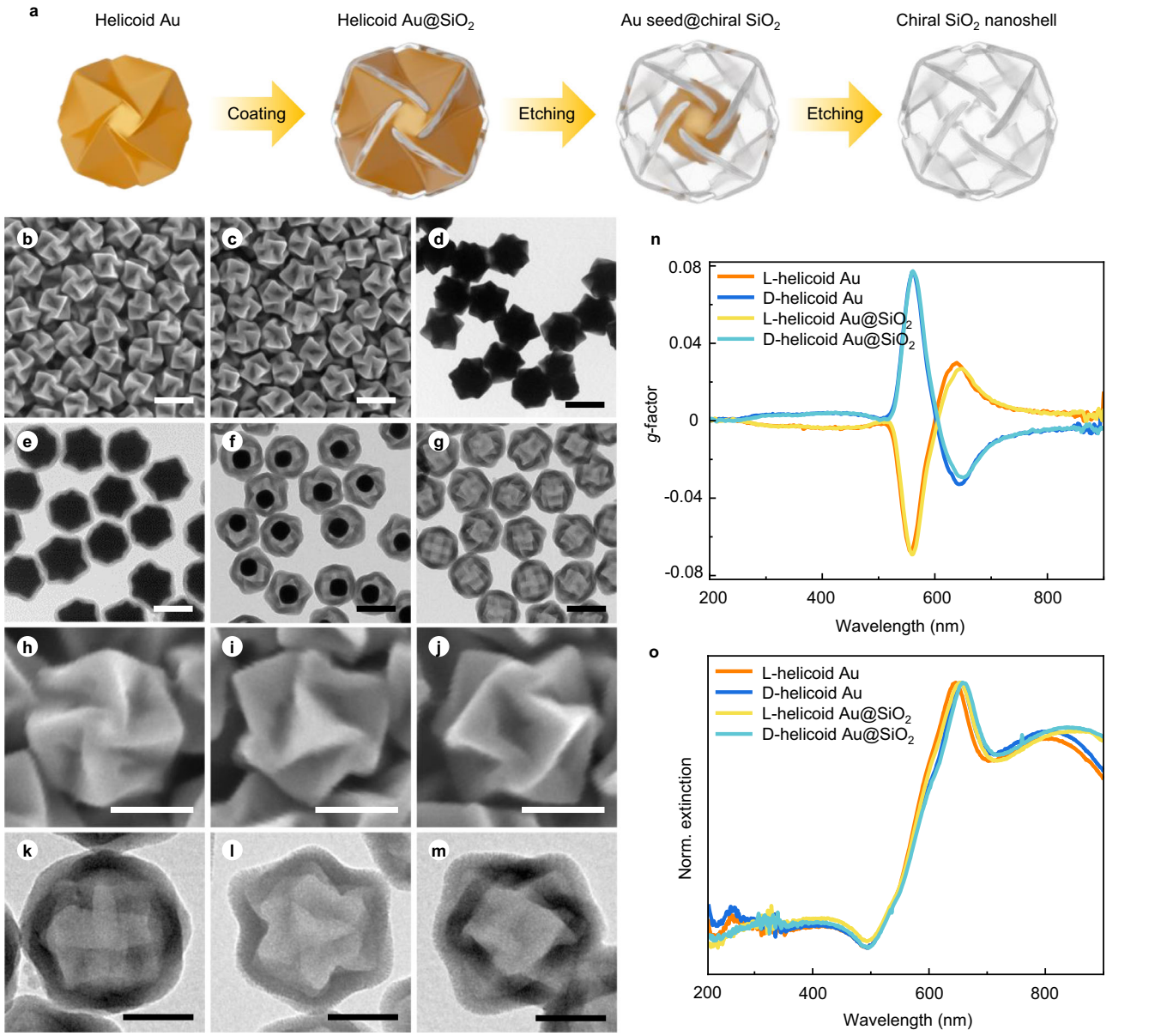

Fig. 2 | Process illustration of chiral nanoconfinement strategy. a Schematic illustration for the formation of silica nanoshells as chiral transfer medium. The golden and translucent models represent the Au NPs and chiral SiO_2 nanoshells, respectively. **b**, **c** SEM images of (**b**) L-helicoid Au NPs and (**c**) D-helicoid Au NPs with the *g*-factor of 0.07. **d**–**g** TEM images of (**d**) L-helicoid Au NPs, (**e**) helicoid Au@SiO_2 NPs, (**f**) Au seed@chiral SiO_2 NPs, and (**g**) chiral SiO_2 nanoshells. **h**–**m** SEM images of individual 0.07-L-helicoid Au NP oriented along the (**h**) [100], (**i**) [111], and (**j**) [110] axes. TEM images of individual 0.07-L-chiral SiO_2 nanoshells viewed from the (**k**) [100], (**l**) [111], and (**m**) [110] axes. **n**, **o**, (**n**) *g*-factor and (**o**) normalized extinction spectra of L- (orange) and D-helicoid Au NPs (blue), L- (yellow) and D-helicoid Au@SiO_2 NPs (sky blue). Scale bars: **b**–**g** 200 nm. **h**–**m** 100 nm. Source data are provided as a Source Data file.

pyramids[47] (Fig. 2b, c). Taking the L-helicoid Au induced by L-Cys as an example, the misalignment of four ridges from different trigonal pyramids leads to a counterclockwise rotated pinwheel-like structure, as viewed in the [100] direction (Fig. 2h). Each trigonal pyramid of the helicoid Au NPs exhibits a distinct counterclockwise rotation along the [111] axis (Fig. 2i). Viewed from the [110] direction, the synchronized rotation of two trigonal pyramids creates a tilted valley (Fig. 2j). In the present of D-Cys, pinwheel-like structures and trigonal pyramids of D-helicoid Au NPs display clockwise rotation (Supplementary Fig. 1). By controlling the amounts of seeds, the size of helicoid NPs and the depth of valleys can be adjusted (Supplementary Figs. 2 and 3), accompanied by the change of dissymmetry factor (*g*-factor), up to 0.14 (Supplementary Fig. 4).

To obtain chiral SiO_2 nanoshells, the helicoid Au NPs are coated with a ≈ 22.5 nm thick silica shell through base-catalyzed hydrolysis of tetraethyl orthosilicate (TEOS)[58,59] (Fig. 2e). Subsequently, the helicoid Au templates can be partially or completely removed through H_2O_2 etching[60] (Fig. 2f, g). Figure 2k–m show the transmission electron microscopy (TEM) images of the chiral SiO_2 nanoshells viewed along different directions, demonstrating a complete replication of the complex chiral structures of the helicoid Au NPs. The coating and etching processes are monitored by circular dichroism (CD, Fig. 2n and Supplementary Fig. 5a) and UV-vis (Fig. 2o and Supplementary Fig. 5b) spectroscopy. After coating with silica shells, the chiroptical properties experience a slight red-shift, which is attribute to the slightly higher refractive index of SiO_2 ($n = 1.46$) compared to H_2O ($n = 1.33$)[61,62]. The CD signals of L- and D-helicoid Au@SiO_2 NPs are inverted with respect to each other, consistent with the helicoid Au NPs (Fig. 2n). After partial or complete etching of Au, the CD signal will completely disappear (Supplementary Fig. 5a). In addition, statistical analysis of three

batches of helicoid Au@SiO_2 NPs shows that nearly 100% of the helicoid Au NPs are coated with uniform, crack-free SiO_2 nanoshells (Supplementary Fig. 6), and 98.3% of the empty chiral SiO_2 nanoshells remain intact after etching (Supplementary Fig. 7).

A shape-replicating growth pathway

The chiral SiO_2 nanoshells are subsequently employed as chiral nanocontainers for the growth of different helicoid metal NPs. By optimizing the reaction conditions, the chiral nanoconfinement from chiral SiO_2 nanoshells can transfer their chirality to helicoid Pt, Au@Pt, and Au@Pd NPs, which strictly replicate the chiral morphology of the SiO_2 nanoshells.

Enantioselective growth of helicoid Pt NPs

To grow helicoid Pt NPs within the chiral nanoshells, Pt seeds are first introduced inside chiral nanoshells as nucleation centers to minimize the risk of non-specific or untemplated growth (Fig. 3a and Supplementary Fig. 8). This can be achieved by depositing a small quantity of Pt onto Au seeds which are obtained by partially etching helicoid Au NPs, employing K_2PtCl_4 as the metal precursor and L-ascorbic acid (AA) as the reducing reagent (Fig. 3b). The Au seeds are subsequently removed by Au^{3+}, leaving Pt seeds confined within the chiral nanoshells (Fig. 3c). Ultimately, helicoid Pt@SiO_2 NPs can be acquired by the growth of Pt seeds confined in the chiral silica nanoshells by optimizing growth time (Fig. 3d). Helicoid Pt NPs can be obtained after the removal of silica shells by NaOH (Fig. 3e).

Under optimum conditions, L- or D-helicoid Pt NPs with a purity of 93.3% and a size distribution of 209.2 ± 6.6 nm can be obtained (Fig. 3f, g and Supplementary Fig. 9). They exhibit identical enantiomeric helicoid structures as the L- or D-helicoid Au NPs. When viewed from different directions, L- or D-helicoid Pt NPs showcase counterclockwise or clockwise rotated pinwheel-like features and trigonal pyramids, and oppositely tilted valleys (Fig. 3j–l and 3n–p), suggesting the helicoid Pt NPs strictly replicate the chiral morphologies of the helicoid Au NPs, due to the steric hindrance imposed by the chiral silica nanoshells. The selected area electron diffraction (SAED) pattern on a single helicoid Pt NP (Fig. 3r), characterized by typical diffraction rings, illustrates that Pt grows into a polycrystalline structure[63]. High-resolution TEM (HRTEM) study (Fig. 3s) reveals abundant crystal domains with different lattice orientations, confirming the polycrystalline nature of the helicoid Pt NPs. High-angle annular dark-field scanning transmission electron microscopy (HAADF-STEM) image and energy-dispersive X-ray spectroscopy (EDX) elemental mapping (Fig. 3t) confirm the uniform distribution of Pt over the helicoid Pt NPs. Furthermore, X-ray diffraction (XRD) (Supplementary Fig. 10) and X-ray photoelectron spectroscopy (XPS) patterns (Supplementary Fig. 11) prove the formation of metallic and crystalline Pt NPs.

The growth route of helicoid Pt NPs (Fig. 1, Route I) is monitored by TEM studies (Supplementary Fig. 12). In the early stage, the Pt seeds slowly grow into irregular shapes and more than one Pt NPs can be observed with one nanoshell. With the increase in size, the Pt NPs in each nanoshell emerge into one NP and begin to exhibit the helicoid structure by the steric hindrance imposed by the chiral silica nanoshells. At an optimal reaction time of 75 min, the Pt NPs filled all the space within silica nanoshells and L- or D-helicoid Pt NPs with a purity of 93.3% could be obtained after SiO_2 removal (Supplementary Fig. 13). With the extension of reaction time, multiple small disordered polycrystalline Pt NPs are attached to the outer surface of the chiral Pt NPs. Furthermore, the chiral nanoconfinement strategy has the capability for scale-up production. The synthesis can be scaled up to 125 times, yielding ≈15 mg of helicoid Pt NPs (Supplementary Fig. 14). In addition, similar growth conditions can also be applied for the preparation of helicoid Au@Pt NPs by directly using Au seeds as nucleation centers (Supplementary Fig. 15), demonstrating the versatility of the chiral nanoconfinement strategy in synthesizing helicoid NPs with either pure or core-shell Pt-based structures.

Interestingly, the helicoid Pt NPs display notable chiroplasmonic properties. The L- and D-helicoid Pt NPs exhibit distinct inverted chiroptical signals with a *g*-factor of ≈0.0007 at about 445 nm (Fig. 3h). Similar chiroplasmonic properties can be observed from the helicoid Au@Pt NPs as well (Supplementary Fig. 16). The consistent CD spectra of helicoid Pt and helicoid Au@Pt NPs demonstrate that the Au core has minimal influence on the chiroptical properties of the helicoid Pt-based NPs. To understand the chiroplasmonic properties of helicoid Pt NPs, the finite-difference time-domain (FDTD) method is employed to simulate their chiroptical properties (Supplementary Fig. 17). The overall spectra in the simulations are consistent with the experimental results, despite differences in *g*-factors possibly due to the model's assumption of smooth surfaces for the Pt-based NPs, whereas the actual samples exhibit surface roughness (Fig. 3q, s). Furthermore, the intensity difference distribution for the local electric fields of L- or D-helicoid Pt (Fig. 3i, m) upon plasmonic excitation is simulated, consistent with the rotational direction of the pinwheel-like geometry of the L- or D-Pt NPs, respectively. These results suggest the potential of the helicoid shape to impart chiroptical properties to nanomaterials composed of non-coinage metals.

Enantioselective growth of helicoid Au@Pd NPs

The chiral nanoconfinement strategy can be extended for the enantioselective synthesis of helicoid Pd-based NPs (Fig. 4a). In order to initiate the growth of Pd within the confined space of silica nanoshells, H_2PdCl_4 as a metal precursor and AA as a reducing agent are introduced into the Au seed@SiO_2 solution. As shown in Fig. 4b–i, L- and D-helicoid Au@Pd also exhibit distinct mirror-symmetric helicoid morphologies with oppositely rotating pinwheel-like structures. The three-dimensional (3D) structures of the helicoid Au@Pd NPs are also reconstructed through electron tomography, revealing chiral features consistent with scanning electron microscopy (SEM) observations (Supplementary Fig. 18). The helicoid Au@Pd NPs exhibit relatively stronger chiroptical properties compared to the helicoid Pt NPs, with a *g*-factor of ≈0.0029 (Fig. 4j). FDTD simulation results (Supplementary Fig. 19) are in good agreement with the experimental results, and there is no difference in the optical signal of helicoid Pd-based NPs with or without Au cores, indicating that the chiroptical signal originate from the helicoid Pd shells. Furthermore, FDTD simulations demonstrate that the properties and relative positions of metal cores have minimal impact on the chiroplasmonic properties of helicoid core-shell structures, whereas the plasmonic properties of the shells strongly influence the chiroplasmonic behavior. The intensity sequence aligns with the classical trend of plasmonic properties[64] (Supplementary Figs. 20–22). HAADF-STEM image (Fig. 4k), EDX elemental mapping (Fig. 4l–n), EDX linear scan profiles (Fig. 4o) collectively provide evidence for an Au@Pd core-shell structure. XPS (Supplementary Fig. 23) and XRD results (Supplementary Fig. 24) prove the formation of metallic and crystalline Pd nanoshells on Au seeds. TEM, SAED, and HRTEM studies of a single helicoid Au@Pd NP (Fig. 4p–r) show that Pd also grows into a polycrystalline structure on the Au seed.

Although both Pt- and Pd-based helicoid NPs follow the shape-replicating pathway, their growth routes are different. In contrast to the Pt-based helicoid NPs, where purity is sensitive to the optimum reaction time, the purity of the Pd-based helicoid NPs can be effectively controlled by the amount of seeds added (Fig. 1, Route II). Introducing an excessive amount of seeds results in some nanoshells being completely filled while others remain partially empty (Supplementary Fig. 25). When 0.27 mL of seed solution was added, half of the nanoshells remain unfilled. As seed addition decreased, the percentage of fully filled nanoshells increases. Upon reducing the seed quantity to one-third, helicoid Au@Pd NPs with a purity of 96.2% and a diameter of 213.3 ± 6.9 nm (Supplementary Fig. 26) are obtained, which reproduce

https://doi.org/10.1038/s41467-025-57624-w

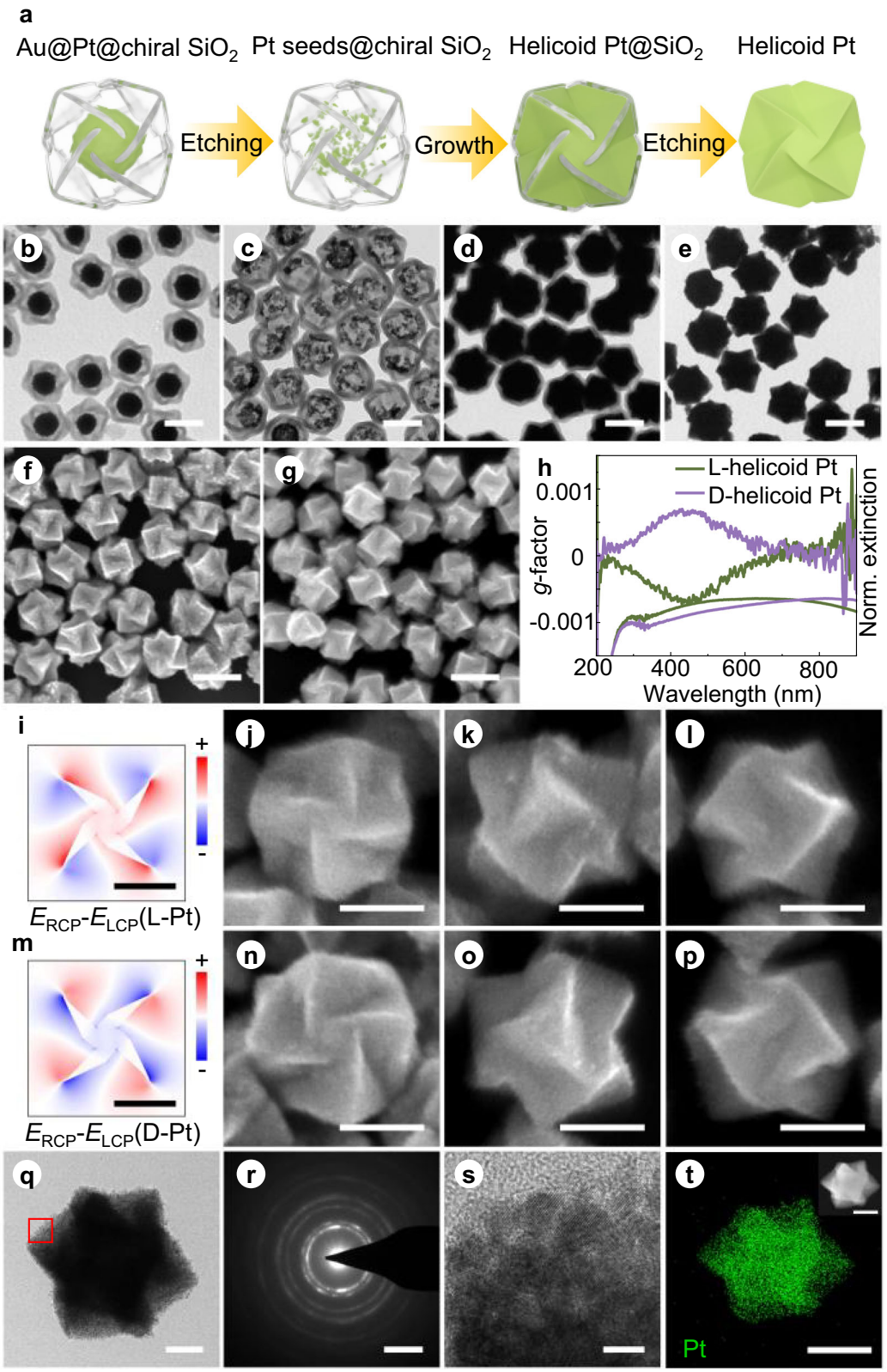

Fig. 3 | The enantioselective synthesis of helicoid Pt NPs. a Schematic illustration for the synthesis of helicoid Pt NPs. The green and translucent models represent the Pt-based NPs and chiral SiO_2 nanoshells, respectively. **b**–**e** TEM images of (**b**) Au@Pt@chiral SiO_2 NPs, (**c**) Pd seeds@chiral SiO_2 NPs, (**d**) L-helicoid Pt@SiO_2 NPs, and (**e**) L-helicoid Pt NPs. **f**, **g** SEM images of (**f**) L- and (**g**) D-helicoid Pt NPs. **h** The *g*-factor and normalized extinction spectra of L- (dark green) and D-helicoid Pt NPs (violet). **i**–**p** Theoretical calculation of the intensity difference distribution of local electric fields ($\Delta E = E_{RCP}$-E_{LCP}) on (**i**) L- and (**m**) D-helicoid Pt NPs irradiated by circularly polarized light from the [100] direction, with the color map from blue (−2.0) to red (2.0). SEM images of individual (**j**–**l**) L- and (**n**–**p**) D-helicoid Pt NPs viewed from the (**j**, **n**) [100], (**k**, **o**) [111], and (**l**, **p**) [110] axes. **q**, **r** (**q**) TEM image of a single helicoid Pt NP and (**r**) the corresponding SAED pattern taken over the entire NP. **s** HRTEM image of the edge-on surface on the helicoid Pt NP corresponding to the red box in (**q**). **t** EDX elemental mapping of Pt (green) from a single helicoid Pt NP. The inset show the corresponding HAADF-STEM image. Scale bars: **b**–**g** 200 nm. **i**–**p** 100 nm. **q** 50 nm. **r** 5 nm^{-1}. **s** 5 nm. **t** 100 nm. Source data are provided as a Source Data file.

https://doi.org/10.1038/s41467-025-57624-w

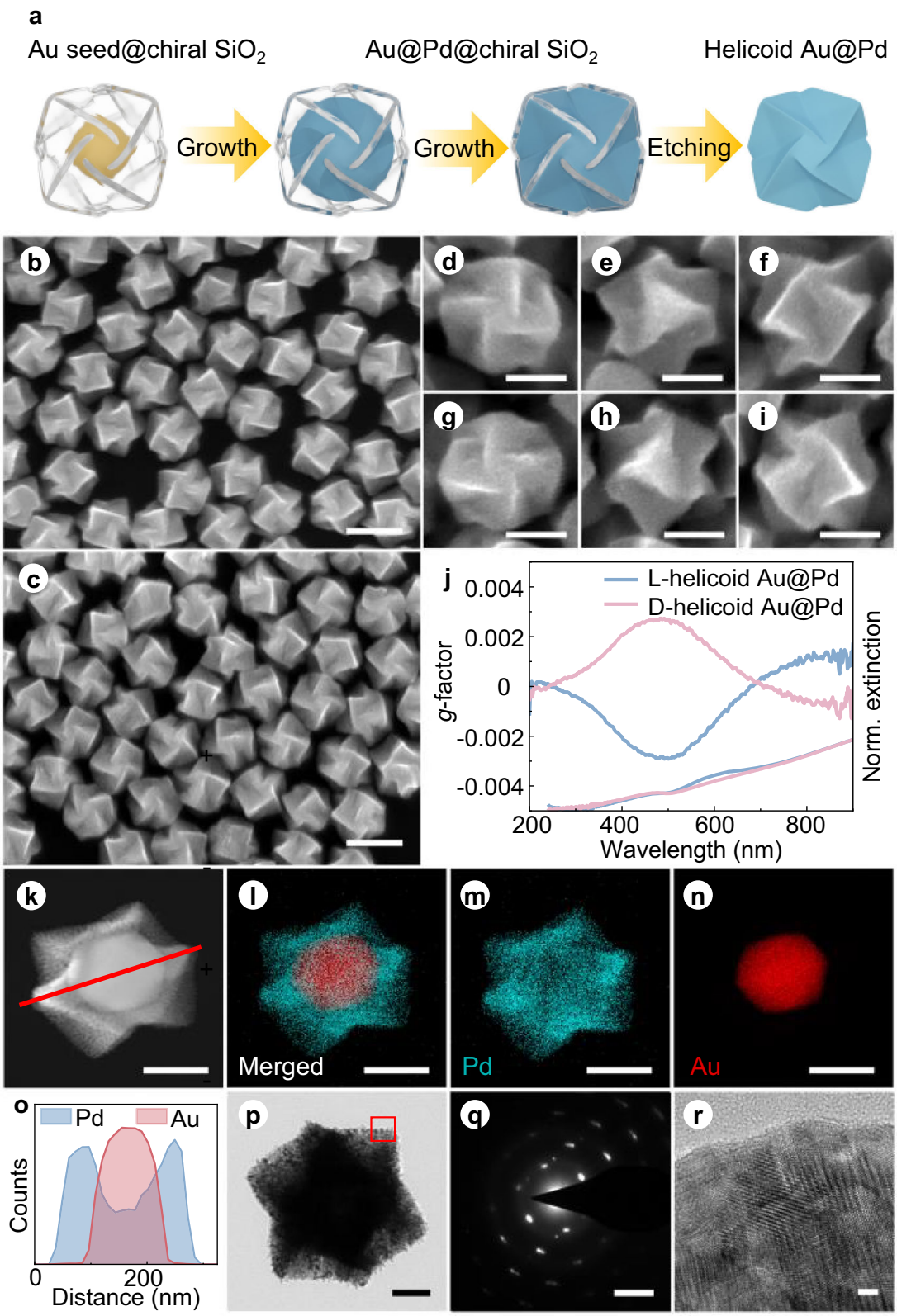

Fig. 4 | The enantioselective synthesis of helicoid Au@Pd NPs. a Schematic illustration for the synthesis of helicoid Au@Pd NPs. The yellow, blue, and translucent models represent the Au NP, Pd-based NPs, and chiral SiO_2 nanoshells, respectively. **b**, **c** SEM images of (**b**) L- and (**c**) D-helicoid Au@Pd NPs. **d**–**i** SEM images of individual (**d**–**f**) L- and (**g**–**i**) D-helicoid Au@Pd NPs viewed from the (**d**, **g**) [100], (**e**, **h**) [111], and (**f**, **i**) [110] axes. **j** The *g*-factor and normalized extinction spectra of L- (blue) and D-helicoid Au@Pd NPs (pink). **k**–**o**, (**k**) HAADF-STEM image and (**l**–**n**) corresponding EDX elemental mapping of a single helicoid Au@Pd NP. The red and blue colors denote Au and Pd, respectively. **o** EDX linear scan profiles of Pd (blue) and Au (red) corresponding to the red line in (**k**). **p**–**r** TEM image of a single helicoid Au@Pd NP, (**q**) corresponding SAED pattern, and (**r**) HRTEM image of edge-on surface corresponding to the red box in (**p**). Scale bars: **b**, **c** 200 nm. **d**–**i** 100 nm. **k**–**n** 100 nm. **p** 50 nm. **q** 5 nm^{-1}. **r** 2 nm. Source data are provided as a Source Data file.

the helicoid morphology of the chiral templates (Supplementary Fig. 27).

To explore the generality of the chiral nanoconfinement strategy, chiral resorcinol-formaldehyde (RF) nanoshells are also employed as the chiral transfer medium for the synthesis of helicoid NPs (Supplementary Fig. 28). Following the procedures established by Yin and coworkers[65,66], chiral RF nanoshells and Au seed@chiral RF NPs are also synthesized (Supplementary Fig. 28b–i). Unlike SiO_2, RF nanoshells offer enhanced stability under harsh conditions such as high temperatures and acidic or basic environments[67], expanding the versatility of our strategy. As a proof of concept, RF nanoshells were used for the growth of Cu-based helicoid NPs, a process that requires harsh conditions—such as the use of hydrazine as a reducing agent—that would degrade SiO_2 nanoshells but are tolerated by RF nanoshells[48]. TEM, EDX, CD, and FDTD simulations collectively confirm the formation of chiroplasmonic helicoid Au@Cu@RF NPs (Supplementary Fig. 29).

A self-adjusting regioselective growth pathway

Based on the principle of chiral nanoconfinement strategy, the chiral induction process can be decoupled from ligand-mediated growth process, thus, it is possible to fine-tune the crystal growth process of NPs. For the growth of Ag in chiral nanoshells, Ag can coat Au seeds in a single-crystalline manner due to the high lattice match between Au and Ag[68]. Simultaneously, the crystal facets of Ag can be governed by introducing ligands favoring {100} or {111} facets. Under chiral confinement, this growth pathway renders this strategy more versatile and flexible, facilitating the generation of alternative chiral helicoid shapes with highly tunable chiroplasmonic properties.

Enantioselective growth of cube-helicoid Au@Ag NPs

The self-adjusting regioselective growth pathway is first demonstrated with the growth of helicoid Au@Ag NPs under the condition that favors the formation of Ag {100} facets. Typically, the growth of Au seeds within the chiral nanoshells is initiated with $AgNO_3$ as a metal precursor, AA as a reducing agent, and polyvinylpyrrolidone (PVP, $M_w \approx 55{,}000\ g\ mol^{-1}$) as stabilizer that promotes the Ag {100} facets[69,70]. Acetonitrile is introduced to form complexes with Ag^+ as a means to control the reaction rate[71]. Without chiral confinement, such a condition would lead to the formation of cubic Au@Ag NPs. In the presence of chiral nanoshells, helicoid Au@Ag NPs with alternative chiral shapes, distinctly different from the chiral templates, are obtained (Fig. 5a–i). Although the helicoid Au@Ag NPs retain a simpler cube-like profile compared to the original chiral Au templates due to intrinsic limitations of nanoconfinement, these results suggest that the chiral nanoconfinement strategy offers an approach to control chiral morphologies beyond the original templates. Due to the combination of four tilted valleys on the edge of cube, L- or D-helicoid Au@Ag NPs present a different pinwheel-like structure rotating counterclockwise or clockwise on the (100) plane, respectively, along the [100] direction (Fig. 5c, f). When viewed from the [111] direction, a clockwise or counterclockwise rotated misalignment of three valleys for L- or D-Au@Ag NP can be observed, respectively (Fig. 5d, g). The valleys with opposite tilts are more clearly observed on the edges of L- or D-helicoid Au@Ag NPs as viewed from the [110] direction (Fig. 5e, h). Single-particle TEM images (Fig. 5j), corresponding SAED patterns obtained on the entire NP (Fig. 5k and Supplementary Fig. 30), and HRTEM study (Fig. 5l and Supplementary Fig. 31) of the Au@Ag@SiO_2 NPs suggest that the growth of Ag leads to a single-crystalline structure. HAADF-STEM image, EDX elemental mapping, and EDX linear scan profiles (Fig. 5m–o) prove that the helicoid Au@Ag NPs are core-shell structures. XPS (Supplementary Fig. 32) and XRD (Supplementary Fig. 33) studies confirm the bimetallic face-centered cubic (FCC) phase of the helicoid Au@Ag NPs.

The dramatic shape difference between the helicoid Au@Ag and the chiral SiO_2 nanoshells indicates that the growth of helicoid Au@Ag NPs follows a distinctly different growth pathway (Fig. 1, Route III). First, the single-crystalline structure of Au@Ag NPs is facilitated by the high lattice match between Au and Ag. Second, PVP promotes the Ag {100} facets, resulting in the helicoid NPs characterized with a cubic profile. Finally, the most striking feature of this growth pathway is the strict orientation correlation between the chiral nanoshells and the Au@Ag helicoids, where the [111], [100], and [110] axes of the Au@Ag helicoids are highly orientated with the 3-, 4-, and 2-fold axes of the chiral SiO_2 nanoshells, respectively, despite the fact that small Au@Ag NPs move freely within the nanoshells at the early growth stage. As the Au@Ag NPs grow larger, they constantly adjust their relative positions within the shells, ensuring the eight vertices of the cube align precisely to the eight triangular pyramids of the template. Such self-adjusting nature of the NPs allows for the strict regioselectivity provided by the chiral silica nanoshells. Specially, upon contacting the inner edges of the chiral nanoshells, the cubic Au@Ag NPs encounter the steric hindrance effect, preventing the growth of Ag on the edges of the NPs and resulting in a valley on each of edge of helicoid NPs. The valleys with certain tilt angles give rise to the chiral structures of the helicoid Au@Ag NPs, depending on the chirality of the chiral nanoshells. Therefore, the self-adjusting regioselective growth pathway enables the synthesis of new chiral helicoid shapes with a purity of 89.3% and a diameter of 159.7 ± 5.6 nm (Supplementary Figs. 34, 35).

The self-adjusting regioselective growth in the chiral nanoshells provides an alternative method to control the chiroplasmonic properties of the helicoid Au@Ag NPs by controlling their sizes and valley depths. For instance, helicoid Au NPs with different *g*-factors (Fig. 2i, j and Supplementary Figs. 1-4) are synthesized as templates for controlling the size of the chiral SiO_2 nanoshells. Using these nanoshells (Fig. 2f and Supplementary Fig. 36), helicoid Au@Ag NPs with different sizes and valley depths are obtained (Fig. 5b–i and Supplementary Figs. 37, 38). As the sizes of chiral templates increase, the sizes of the helicoid Au@Ag NPs increase with deeper valleys, resulting in the pinwheel-like structures. The *g*-factor of Au@Ag NPs, synthesized from SiO_2 nanoshells obtained from helicoid Au NPs with *g*-factor of 0.14, 0.07, and 0.04, can reach approximately 0.08, 0.04, and 0.004, respectively, with λ_{max} (the wavelength at which the maximum *g*-factor is observed) from 491 to 424 nm (Fig. 5p–r). Furthermore, the valley depths and sizes can also be regulated by controlling the amount of Au seed@SiO_2. The *g*-factor obviously increases with the deepening of valleys, but it drops significantly as the depths become shallower, even with an increase of the NP size (Supplementary Figs. 39, 40). Thus, the valley depths of helicoid Au@Ag NPs have a profound effect on their chiroplasmonic properties than sizes.

Enantioselective growth of octahedron-helicoid Au@Ag NPs

Under the self-adjusting regioselective growth pathway, exotic chiral shapes can be obtained with the formation of other crystal facets. When PVP is replaced with citric acid (CA) as the stabilizing agent, which favors the formation of Ag {111} facets[72,73], helicoid Au@Ag NPs with octahedral profiles can be simply synthesized (Fig. 6a–c). Viewed from the [100] axis, the pinwheel-like structures of L- or D-octahedron-helicoid Au@Ag NPs, originating from the combination of four valleys along the four edges extending from the same vertex, which rotate counterclockwise or clockwise with the 4-fold vertex as the rotation center (Fig. 6h, i). This differs from the cube-helicoid Au@Ag NPs, where the pinwheel-like structures originate from four tilted valleys located on the four edges around one square (100) plane (Fig. 5c–h). Furthermore, when viewed from [111] direction, three misaligned valleys rotating on the octahedron-helicoid Au@Ag NPs share the same (111) plane (Fig. 6j–m). Additional details (Supplementary Figs. 41, 42) and electron tomography reconstructions (Supplementary Figs. 43, 44) confirm the helicoid structures of the Au@Ag NPs observed in the SEM images. For completeness, 3D reconstructions of helicoid NPs involved are provided as Supplementary Movies 1–6. The growth of

https://doi.org/10.1038/s41467-025-57624-w

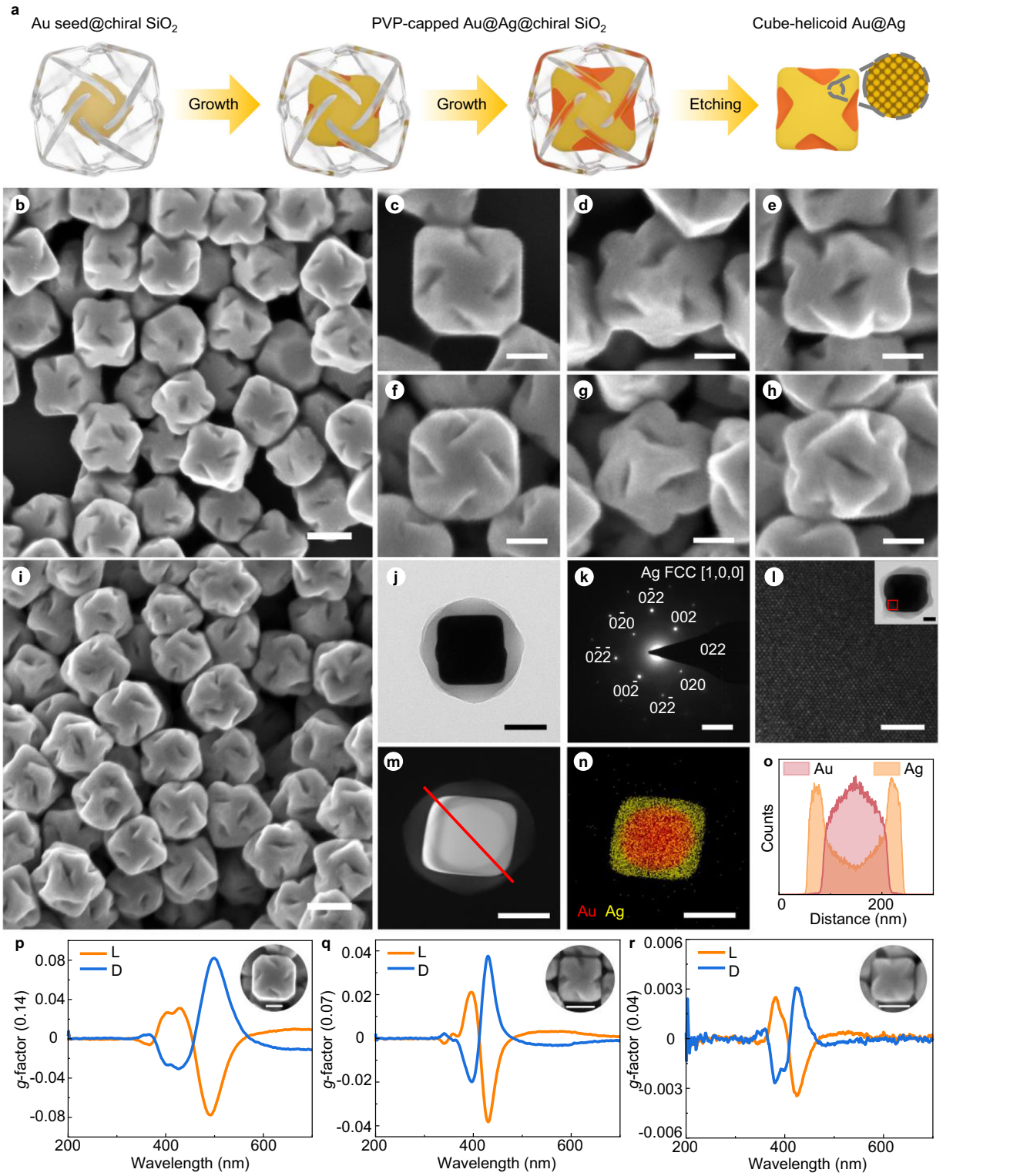

Fig. 5 | The enantioselective synthesis of cube-helicoid Au@Ag NPs. a Schematic illustration for the synthesis of cube-helicoid Au@Ag NPs. The yellow, orange, and translucent models represent the Au NP, Ag-based NPs with cubic profiles, and chiral SiO_2 nanoshells, respectively. **b**, **i** SEM images of (**b**) 0.14-L- and (**i**) 0.14-D-helicoid Au@Ag NPs, respectively. **c**–**h** SEM images of individual (**c**–**e**) 0.14-L- and (**f**–**h**) 0.14-D-helicoid Au@Ag NP viewed from the (**c**, **f**) [100], (**d**, **g**) [111], and (**e**, **h**) [110] axes. **j**, **k**, (**j**) TEM image of a single helicoid Au@Ag@SiO_2 NP along the [100] zone axis, and (**k**) corresponding SAED pattern. **l** HRTEM image of edge-on surface corresponding to the red box in inset. **m**, **n**, (m) HAADF-STEM and (**n**) corresponding EDX elemental mapping of a single helicoid Au@Ag@SiO_2 NP. The red and yellow colors denote Au and Ag, respectively. **o** EDX linear scan profiles of Au (red) and Ag (orange) corresponding to the red line in (**m**). **p**–**r** The *g*-factor spectra of cube-helicoid Au@Ag NPs synthesized using helicoid Au templates with different *g*-factors. (**p**) 0.14, (**q**) 0.07, and (**r**) 0.04 represent the *g*-factor of helicoid Au templates used for synthesis, respectively. (L-helicoid Au@Ag: orange line, D-helicoid Au@Ag: blue line). Scale bars: **b**, **i** 200 nm. **c**–**j** 100 nm. **k** 5 nm^{-1}. **l** 3 nm. Inset: 50 nm. **m**, **n** 100 nm. **p**–**r** 100 nm. Source data are provided as a Source Data file.

https://doi.org/10.1038/s41467-025-57624-w

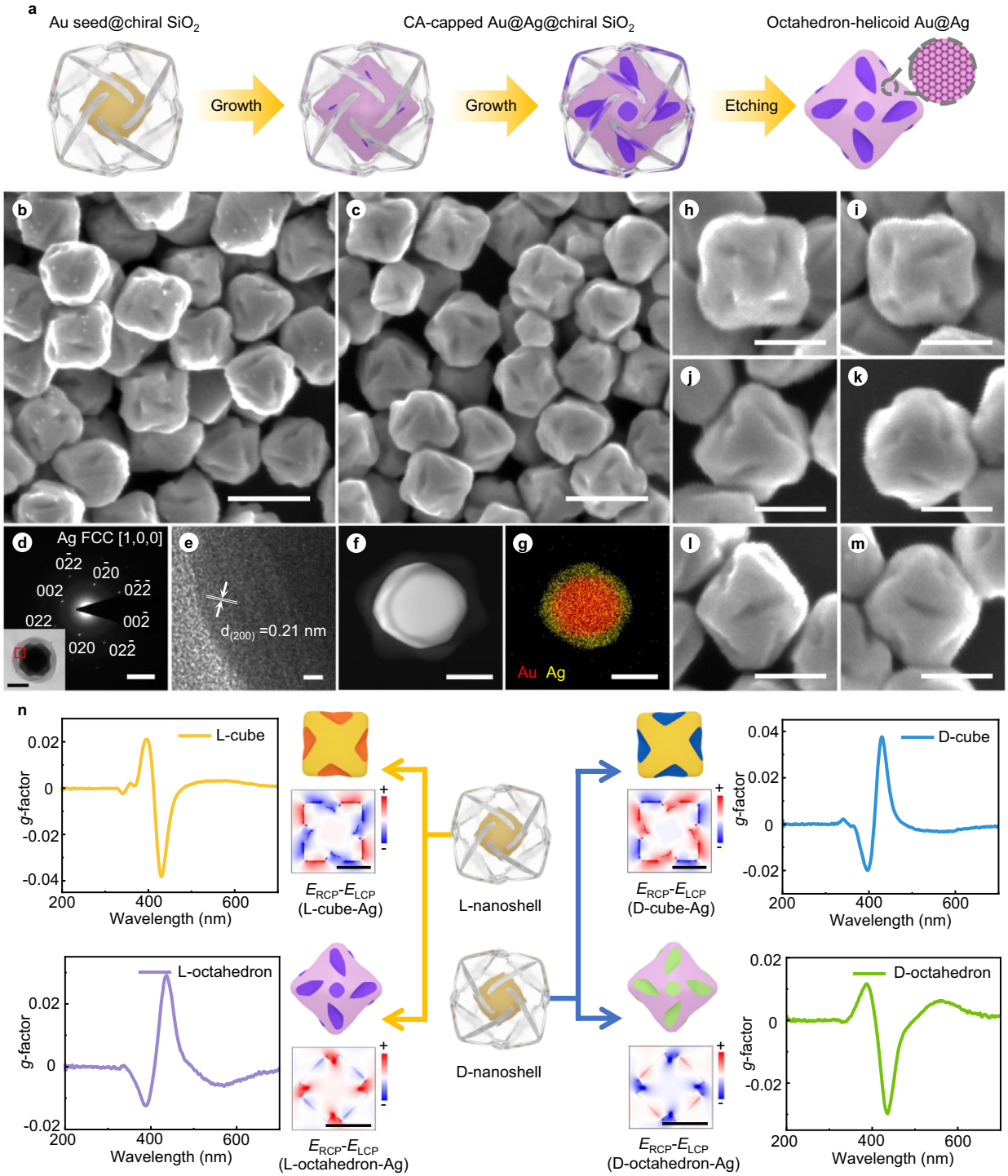

Fig. 6 | The enantioselective synthesis of octahedron-helicoid Au@Ag NPs. **a** Schematic illustration for the synthesis of octahedron-helicoid Au@Ag NPs. The yellow, pink, and translucent models represent the Au NP, Ag-based NPs with octahedral profiles, and chiral SiO_2 nanoshells, respectively. **b**, **c** SEM images of (**b**) 0.07-L- and (**c**) 0.07-D-octahedron-helicoid Au@Ag NPs. **d** SAED pattern of a single octahedron-helicoid Au@Ag@SiO_2 NP along the [100] zone axis. **e** HRTEM image of edge-on surface corresponding to the red box in inset of (**d**). **f** HAADF-STEM and (**g**) corresponding EDX elemental mapping of a single octahedron-helicoid Au@Ag@SiO_2 NP. The red and yellow colors denote Au and Ag, respectively. **h**–**m** SEM images of individual (**h**, **j**, **l**) 0.07-L- and (**i**, **k**, **m**) 0.07-D-octahedron-helicoid Au@Ag NP viewed from (**h**, **i**) [100], (**j**, **k**) [111], and (**l**, **m**) [110] axes. **n** Chiroptical signal reversal of helicoid Au@Ag NPs within the same chiral template regulated by the facet formation. The *g*-factor spectra and geometric models, and the corresponding intensity difference distribution of local electric fields of L- (orange line, orange model with red-orange concaves) and D-cube-Au@Ag NPs (blue line, orange model with blue concaves), L- (purple line, pink model with purple concaves), and D-octahedron-Au@Ag NPs (green line, pink model with green concaves). The intensity difference distributions of local electric fields are presented with the color map from blue (−2.0) to red (2.0). Scale bars: **b**, **c** 200 nm. **d** 5 nm^{-1}. Inset: 100 nm. **e** 2 nm. **f**, **g** 100 nm. **h**–**n** 100 nm. Source data are provided as a Source Data file.

octahedron-Au@Ag NPs follows a single-crystalline core-shell mode with FCC phase, as indicated in TEM, SAED, and EDX studies (Fig. 6d–g and Supplementary Fig. 45). The rigidly aligned orientation of the octahedral Au@Ag NPs with their chiral nanoshells suggests the same self-adjusting regioselective growth pathway (Fig. 1, Route IV). The six vertices of octahedral Au@Ag NPs align with the centers of six pinwheel-like structures of the SiO_2 nanoshells. Consequently, each edge in contact with the nanoshell is constrained during growth, forming a valley with a distinct tilt. Under this pathway, the synthesized octahedron-helicoid Au@Ag NPs exhibit a purity of 88.7% and a size distribution of 177.1 ± 5.0 nm (Supplementary Fig. 46).

The versatility of the self-adjusting regioselective growth pathway is also reflected in governing the chiroplasmonic properties of helicoid Au@Ag NPs. Interestingly, the CD spectra of L-octahedron-Au@Ag NPs and L-cube-Au@Ag NPs show a distinct inversion, despite being synthesized with SiO_2 nanoshells of the same chirality. As shown in Fig. 6n, the CD spectrum of L-octahedron-helicoid Au@Ag NPs exhibits two peaks at around 435 (+) and 388 (-) nm, opposite to the CD spectrum of L-cube-helicoid Au@Ag NPs, where the peaks are located at approximately 430 (-) and 395 (+) nm. A similar signal inversion is observed in two D-helicoid Au@Ag nanostructures obtained through D-chiral nanoshells. To elucidate the phenomenon of chiral inversion, we have conducted FDTD simulations on octahedron- and cube-helicoid Au@Ag NPs. In both cases, the simulated CD and extinction spectra closely match the experimental results (Supplementary Figs. 47, 48). We note that the *g*-factors of the as-synthesized helicoid Ag-based NPs are smaller than those of the original helicoid Au NPs. To investigate this observation, FDTD simulations were conducted on helicoid Ag-based NPs with the same chiral shapes as the original helicoid Au NPs (Supplementary Fig. 49a, b). The results confirm that helicoid Ag-based NPs with these original chiral shapes exhibit higher *g*-factors than the helicoid Au NPs, suggesting that the observed lower *g*-factor of helicoid Ag-based NPs is due to morphological variations. Furthermore, FDTD simulations were performed on helicoid Au NPs with the cubic and octahedral profiles observed in the helicoid Ag-based NPs (Supplementary Fig. 49c, d). The simulations reveal that the *g*-factors of both cube- and octahedron-helicoid Au NPs are indeed lower than those of the corresponding helicoid Ag-based NPs. These confirm that the relatively lower *g*-factors of helicoid Ag-based NPs are primarily due to changes in chiral morphology. The comparatively shallower plasmonic gaps in the helicoid Ag-based NPs are responsible for their reduced *g*-factors[7].

Furthermore, we illustrate the intensity difference distributions of their electric fields ($\Delta E = E_{RCP}$-E_{LCP}) (Fig. 6n) on the helicoid Ag-based NPs when irradiated by right-handed and left-handed circularly polarized light (E_{RCP}, E_{LCP}) (Supplementary Fig. 50). The chiral valleys in L-octahedron- and L-cube-Au@Ag NPs exhibit ΔE with opposite signs, resulting in an overall positive ΔE for the former and an overall negative ΔE for the latter, despite having the same rotation direction. This trend is also observed for two D-helicoid Au@Ag NPs. These findings suggest that the spatial arrangement of chiral units significantly influences their chiroplasmonic properties and can lead to reversed CD signals, in addition to the rotation direction of the chiral units. Currently, reversals of chiroplasmonic properties in chiral nanomaterials using chiral inducers of the same handedness—particularly in Au systems—have been achieved through the hybridization of bichiral centers[7,27,74,75] or by tuning the crystallinity of nanorod seeds[57]. In contrast, our work introduces an alternative route for inducing chirality reversal by precisely controlling crystal facets.

Discussion

In summary, a chiral nanoconfinement strategy has been established for the enantioselective synthesis of chiral NPs. This strategy addresses the limitations associated with previous chiral ligand-directed methods[37,76] by allowing for the decoupling of ligand-mediated crystal growth and chiral induction processes. Consequently, it enables the synthesis of a series of helicoid metal NPs, thereby expanding the scope of available chiral nanomaterials. Moreover, the demonstrated growth pathways under chiral nanoconfinement not only facilitate the precise transfer of chiral morphology from nanoshells to other metals but also yield alternative chiral shapes by integrating other advanced crystal growth strategies. Furthermore, the application of the nanoconfinement synthetic strategy has led to the discovery of a diverse array of chiroplasmonic NPs, highlighting the potential of helicoid shapes in endowing the chiroptical properties of nanomaterials[77]. This strategy achieves precise regulation of chiroplasmonic properties and even signal inversion, providing a platform for customizing chiroplasmonic nanomaterials and understanding the role of chiral structures for chiroplasmonic properties. The chiral nanoconfinement strategy enriches the toolbox for designing chiral NPs[78,79], offering promising potential for a variety of applications. This approach can be extended to the synthesis of catalytically active metals, such as Pt- and Pd-based helicoid NPs[80]. Their combination of catalytic and chiroplasmonic properties makes them candidates for enantioselective catalysis and circularly polarized light (CPL)-enhanced catalysis[81–84]. Additionally, the ability to precisely control the surface facets of Ag helicoid NPs unlocks opportunities for surface-sensitive chiroplasmonic applications in metamaterials[85,86], enantioselective sensing[33,45,87], chiral drug development[88–90], and enantioselective plasmon-enhanced spectroscopy[91,92]. We note that recently, the Nam group reported a versatile method for synthesizing chiral metal helicoids using chiral silica molds[93]. Complementing this work, we propose that decoupling ligand-directed crystal growth from chiral induction can expand the synthetic toolbox for helicoid metal NPs, enabling the formation of alternative chiral shapes from templates or molds. Specifically, our approach provides a pathway for reversing chirality by controlling the chiral shapes and crystal facets of Ag-based NPs using SiO_2 nanoshells with the same chirality. Additionally, we expanded the methodology by replacing SiO_2 with RF shells as the chiral transfer medium, facilitating template-based growth under harsh conditions. Overall, these results, along with recent advancements[43,93–96], offer promising avenues for expanding both the variety and functionality of chiral metal NPs for fundamental research and technological applications.

Methods

Materials

Gold chloride trihydrate ($HAuCl_4 \cdot 3H_2O$, 99.9%), sodium borohydride ($NaBH_4$, 99.99%), TEOS (98%), polyacrylic acid (PAA, $M_w \approx$ 2,000 g mol^{-1}), PVP ($M_w \approx$ 55,000 g mol^{-1} and $M_w \approx$ 40,000 g mol^{-1}), CA (≥ 99.5%), potassium tetrachloroplatinate(II) (K_2PtCl_4, 99.99%), and palladium(II) chloride ($PdCl_2$, 99%) were purchased from Sigma-Aldrich. Hexadecyltrimethylammonium bromide (CTAB, >98.0%), PVP ($M_w \approx$ 10,000 g mol^{-1}), cetylpyridinium chloride monohydrate (CPC, > 98%), hexadecylpyridinium bromide hydrate (CPB, >96.0%), AA (> 99%), L-cysteine hydrochloride monohydrate (> 99.0%), and D-cysteine hydrochloride monohydrate (>99.0%) were purchased from TCI. Cupric chloride dihydrate ($CuCl_2 \cdot 2H_2O$) was purchased from Aladdin. Sodium hydroxide (NaOH, ≥ 96%), hydrochloric acid (HCl, 37 wt.% in water), and ammonia ($NH_3 \cdot H_2O$, 25 wt.% in water) were purchased from Beijing Chemical Reagent Company. Silver nitrate ($AgNO_3$, ≥ 99.8%), resorcinol (≥ 99.5%), and formaldehyde (37%) were purchased from Sinopharm Chemical Reagent Co., Ltd. Methanol (≥99.5%), ethanol (≥99.7%), hydrazine hydrate ($N_2H_4 \cdot H_2O$, 50%) and hydrogen peroxide (H_2O_2, ≥ 30.0%) were purchased from Xi Long Scientific Co., Ltd. Acetonitrile (≥99%) was purchased from Tian Tai Chemical Reagent Co., Ltd. All chemicals were used as received without further purification. Ultrapure water was used in all of the experiments.

Synthesis of Au seeds

Single-crystalline Au seeds capped with CPC were prepared according to the procedures from refs. 97,98. with modification:

(1) Synthesis of small Au nanorods: First, the Au seeds for small Au nanorods were synthesized by adding 0.25 mL of 10 mM $HAuCl_4$ and 0.6 mL of 10 mM $NaBH_4$ sequentially to 10 mL of 100 mM CTAB solution under vigorous stirring. After 2 min, the mixture was left undisturbed at 30 °C for at least 30 min. To obtain small Au nanorods, the growth solution was prepared by sequentially introducing 6 mL of 10 mM $HAuCl_4$, 0.72 mL of 10 mM $AgNO_3$, and 0.96 mL of 100 mM AA into 120 mL of 100 mM CTAB solution, with gentle shaking. The growth of small Au nanorods was initiated by rapidly introducing 144 µL of the Au seeds solution. The reaction proceeded at 30 °C for 2 h without disturbance. Then, the product was centrifuged (15,778 × *g*, 10 min), washed once with water, and redispersed in 120 mL of 10 mM CTAB solution.

(2) Growth and etching of larger Au nanorods: To obtain spherical Au seeds, larger Au nanorods were first grown by adding 6 mL of 10 mM $HAuCl_4$ and 1.2 mL of 100 mM AA to 120 mL of the small Au nanorod solution, followed by incubation at 40 °C for 1 h without disturbance. The product was centrifuged (15,778 × *g*, 10 min) and redispersed in 120 mL of 10 mM CTAB solution. Then, the larger Au nanorods were etched by introducing 2.4 mL of 10 mM $HAuCl_4$ into 120 mL of the larger Au nanorod solution. The reaction proceeded at 40 °C for 12–16 h without disturbance. The product was centrifuged (15,778 × *g*, 10 min), washed twice with 20 mM CPC, and redispersed in 120 mL of 20 mM CPC.

(3) Secondary growth and etching of Au NPs: To ensure the monodispersity of the final seeds, secondary growth of Au NPs was carried out by sequentially adding 4 mL of 10 mM $HAuCl_4$, 0.6 mL of 100 mM AA, and 40 mL of the etched Au NPs into 200 mL of 100 mM CPC solution. The reaction solution was left at 30 °C for 1 h without disturbance, then centrifuged (15,778 × *g*, 3 min) and redispersed in 40 mL of 10 mM CTAB solution. The final step was the synthesis of Au nanospheres by adding 2.4 mL of 10 mM $HAuCl_4$ to 120 mL of the Au NP solution obtained after secondary growth, followed by incubation at 40 °C for 12–16 h. The product was centrifuged (15,778 × *g*, 10 min), washed twice with 20 mM CPC, and redispersed in 120 mL of 20 mM CPC.

Synthesis of helicoid Au NPs

Helicoid Au NPs were synthesized using the seed-mediated growth method[47]. The growth solution for the helicoid Au NPs was prepared by sequentially introducing 22.5 mL of 100 mM CPC solution, 67.5 mL of 100 mM CPB solution, 10 mL of 10 mM $HAuCl_4$ solution, and 70 mL of 100 mM AA solution into 101.25 mL of water, with gentle shaking. Subsequently, 0.625 mL of 0.1 mM L- or D-Cys solution (correspond to L- or D-helicoid Au NPs, respectively) was added and thoroughly blended. Finally, the growth of helicoid Au NPs was initiated by rapidly introducing 3 mL of the Au seed solution. The growth continued for 2 h in a 30 °C water bath without disturbance. The resulting products were collected through centrifugation (3944 × *g*, 3 min), washed once with water, and then re-dispersed into 60 mL of 1.5 mM CTAB solution. The *g*-factor of helicoid Au NPs produced by the above procedures is 0.07.

For the synthesis of helicoid Au NPs with other sizes and valley depths, the reactions were carried out using identical reaction conditions, except for the variations in the volume of seeds added. Specifically, 0.75 mL of seeds was added to produce helicoid Au NPs with a *g*-factor of 0.14, while 4.5 mL of seeds was added to yield helicoid Au NPs with a *g*-factor of 0.04.

Synthesis of porous chiral silica nanoshells on helicoid Au NPs

For SiO_2 coating, 0.6 mL of 0.1 M NaOH solution was added into the as-prepared helicoid Au solution under stirring (400 rpm), followed by three additions of TEOS solution (20% v/v in methanol, 0.18 mL) at 60 min intervals. The reaction was stirred in a 30 °C water bath for 96 h to obtain helicoid Au@SiO_2 NPs, coating a silica shell with a thickness of 22.5 nm. The products were collected by centrifugation (7012 × *g*, 3 min), and then washed with water and methanol. Finally, helicoid Au@SiO_2 was re-dispersed into 25 mL of methanol for storage.

To increase the porosity of the silica nanoshell and enhance the condensation within the Si-O-Si network, a heat treatment was performed for the helicoid Au@SiO_2 NPs[99]. Take 3 mL of helicoid Au@SiO_2 stock solution and re-disperse it in 30 mL of PVP solution ($M_w \approx 10{,}000$ g mol^{-1}, 0.013 g mL^{-1}). The solution was then heated at 95 °C for 2 h. Eventually, the products was washed twice with methanol and dispersed in 12 mL of methanol.

Synthesis of RF nanoshells on helicoid Au NPs

Before coating the RF layer, 2.4 mL of the helicoid Au solution was collected by centrifugation and re-dispersed in 1 mL of PAA solution (10 mg mL^{-1}) and incubated for 8 h to modify PAA on the surface of the NPs. The helicoid Au NPs were then re-dispersed in 27 mL of water containing 10 mg of resorcinol, 60 µL of diluted ammonia (2.5 wt.%), and 18 µL of formaldehyde. The solution was stirred in an oil bath at 50 °C for 2 h, then heated to 100 °C for 3 h. After the reaction, the helicoid Au@RF NPs were collected by centrifugation (7,012× *g*, 3 min), washed alternately with water and ethanol, and finally dispersed into 4 mL of water.

Selective etching of Au in helicoid Au@SiO_2 NPs

To obtain the Au seed@chiral SiO_2 NPs, 100 µL of 37 wt.% HCl and 50 µL of 200 mM H_2O_2 solution were added into 5 mL of helicoid Au@SiO_2 solution treated with heat. The reaction was continued in a 70 °C water bath for 30 min with stirring. When the solution was cooled down, the products were collected by centrifugation (15,778 × *g*, 3 min). The synthesized Au seed@SiO_2 NPs were washed with 1.1 wt.% PVP solution ($M_w \approx 55{,}000$ g mol^{-1}), and then redispersed in 1 mL of PVP solution for further synthesis. To obtain the chiral SiO_2 nanoshells, the reaction time was extended to 50 min. In the case of the helicoid Au@RF NPs, the selective etching of Au was continued for 120 min in a 70 °C water bath with stirring.

Synthesis of helicoid Pt@SiO_2 and helicoid Au@Pt@SiO_2 NPs

First, 0.15 mL of seed solution was diluted to 0.6 mL with PVP solution ($M_w \approx 55{,}000$ g mol^{-1}), followed by the addition of 120 µL of 10 mM K_2PtCl_4 solution and 50 µL of 30 mM AA solution. The reaction solution was kept undisturbed in a 30 °C water bath for 30 min. To obtain Pt seeds@chiral SiO_2 NPs, NPs were redispersed into 5 mL of 50 mM CTAB solution, then 50 µL of 5 mM NaI solution and 100 µL of 10 mM $HAuCl_4$ solution were added. The reaction was carried out in a 50 °C water bath for 60 min to achieve complete etching of Au. The Pt seeds@chiral SiO_2 NPs were collected by centrifugation (15,778 × *g*, 3 min), washed with water and then dispersed in 0.6 mL of PVP solution ($M_w \approx 55{,}000$ g mol^{-1}). To obtain the helicoid Pt@SiO_2 NPs, Pt seeds@chiral SiO_2 solution was mixed with 120 µL of 10 mM K_2PtCl_4 solution and 50 µL of 30 mM AA solution. The reaction solution was gently shaken for 5 min and then kept undisturbed in a 30 °C water bath for 75 min. The resulting products were centrifuged at 2739 × *g* for 3 min, washed with ethanol, and redispersed in ethanol.

For the synthesis of helicoid Au@Pt@SiO_2 NPs, 0.15 mL Au seed@chiral SiO_2 solution was diluted to 0.6 mL, followed by the addition of 120 µL of 10 mM K_2PtCl_4 solution and 50 µL of 30 mM AA solution. Finally, the reaction solution was gently shaken for 5 min and then kept undisturbed in a 30 °C water bath for 105 min.

Synthesis of helicoid Au@Pd@SiO_2 NPs

For the growth of Pd, 0.09 mL of seed solution was diluted to 0.6 mL with PVP solution ($M_w \approx 55{,}000$ g mol^{-1}), followed by the addition of 30 µL of 10 mM $PdCl_2$ solution (dissolved in 10 mM HCl solution) and 120 µL of 30 mM AA solution. The reaction solution was gently shaken in a 30 °C water bath for 3 h, and finally the products were collected by centrifugation.

Synthesis of helicoid Au@Cu@RF NPs

For the growth of helicoid Cu-based NPs, 0.16 mL of the Au seed@-chiral RF solution was mixed with 5 mL of H_2O, 0.5 mL of PAA solution (18 mg mL^{-1}), and 0.125 mL of PVP solution ($M_w \approx 40{,}000$ g mol^{-1}, 0.1 g mL^{-1}). Under stirring, 50 µL of 100 mM $CuCl_2$ solution and 90 µL of N_2H_4 solution (50%) were added to the solution successively. The reaction was carried out in a water bath at 25 °C for 20 min, and then heated to 60 °C for 40 min. Finally, the products were collected by centrifugation.

Synthesis of helicoid Au@Ag@SiO_2 NPs

For the growth of Ag, different amounts of seed solutions were diluted to 0.6 mL with PVP solution ($M_w \approx 55{,}000$ g mol^{-1}), followed by the addition of 60 µL of acetonitrile and 30 µL of 10 mM $AgNO_3$ solution. The growth of Ag was initiated by rapidly introducing 25 µL of 30 mM AA solution. Finally, the reaction solution was gently shaken in a 30 °C water bath for 50 min, and then cube-helicoid Au@Ag@SiO_2 NPs were collected by centrifugation.

For the synthesis of octahedron-helicoid Au@Ag@SiO_2 NPs, Au seed@SiO_2 was dispersed in 1 mL of 50 mM CA solution. 0.09 mL of seed solution was diluted to 0.6 mL with CA solution, followed by the addition of 30 µL of 10 mM $AgNO_3$ solution and 25 µL of 30 mM AA solution. Finally, the reaction solution was gently shaken in a 30 °C water bath for 70 min.

Etching of silica nanoshells

To obtain helicoid metal NPs without nanoshells, the reaction solution was prepared by introducing 0.1 mL of 5 wt.% PVP solution ($M_w \approx 10{,}000$ g mol^{-1}) and 0.1 mL of 1 M NaOH solution into 0.8 mL of water. A batch of helicoid metal@SiO_2 NPs was dispersed in 1 mL of the reaction solution and kept in a 30 °C water bath for 1 h. The resulting helicoid metal NPs were collected by centrifugation at 1753 × g for 2 min and washed with water.

Characterization

SEM images were acquired by a Zeiss Merlin microscope at 5 kV. CD spectra were recorded using a Jasco J-820 spectropolarimeter instrument. Extinction spectra were recorded using a Shimadzu UV-1800 UV-vis spectrophotometer. TEM images were obtained using a Japan's Hitachi H-600 TEM operating at 100 kV. EDX data, SAED, HAADF-STEM, and HRTEM images were acquired with Tecnai G2 F30 STWIN operating at 300 kV. XRD data was obtained on Bruker D8 Discover with Cu K_α radiation. XPS spectra was obtained using a thermo ESCALAB 250 spectrometer with an Al Kα X-ray source. 3D electron tomography reconstruction was performed using a Thermo Talos F200X G2 TEM instrument (200 kV) equipped with CMOS camera (Thermo), and the image post-processing used a software package of Inspect 3D and Avizo.

Kuhn's dissymmetry factor (g-factor) is a dimensionless quantity that is used for quantitative comparisons of chiroptical properties among different systems and was calculated from the measured extinction and CD values by Eq. (1):

$$g-\text{factor} = 2\frac{A_L - A_R}{A_L + A_R} \propto \frac{\text{CD}}{\text{extinction}} \quad (1)$$

Numerical simulations

The simulations were performed using the 3D FDTD numerical method with commercial software (FDTD Solution, Lumerical Solutions, Inc.). The theoretical model dimensions matched the statistical results obtained from SEM images, and the material permittivity values were sourced from Johnson and Christy data in the software's database. The background index was set as 1.361 (ethanol). A uniform mesh size of 1 nm was applied in all directions around the model to maintain structural detail, and the boundary conditions were set as perfectly matched layer. Circularly polarized light was modeled as two orthogonal linearly polarized beams with a phase difference of +90° and -90° for left circularly polarized (LCP) and right circularly polarized (RCP) light, respectively. The simulation time was set to 1000 s to ensure the convergence of the results. CD and extinction spectra were calculated based on the average simulations from three different nanoparticle orientations. For chiral nanomaterials with original helicoid Au shapes, three spectra were obtained under irradiation with circularly polarized light along the [100], [110], and [111] directions. For chiral nanomaterials with cube- or octahedron-helicoid Au@Ag shapes, three spectra of NPs were obtained from the three axes in a right-angled coordinate system. Electric field distributions were recorded by frequency domain profile monitor.

Data availability

The data that support the findings of this study are available from the corresponding author upon request. Source data are provided with this paper.

References

1. Subotnik, J. E. Chiral molecules to transmit electron spin. *Science* **382**, 160–161 (2023).
2. Deng, M., Yu, J. & Blackmond, D. G. Symmetry breaking and chiral amplification in prebiotic ligation reactions. *Nature* **626**, 1019–1024 (2024).
3. Rao, Z. et al. Observation of unconventional chiral fermions with long Fermi arcs in CoSi. *Nature* **567**, 496–499 (2019).
4. Li, Z. et al. A magnetic assembly approach to chiral superstructures. *Science* **380**, 1384–1390 (2023).
5. Ma, W. et al. Chiral inorganic nanostructures. *Chem. Rev.* **117**, 8041–8093 (2017).
6. Zheng, G. et al. Discrete metal nanoparticles with plasmonic chirality. *Chem. Soc. Rev.* **50**, 3738–3754 (2021).
7. Lee, H. E. et al. Amino-acid- and peptide-directed synthesis of chiral plasmonic gold nanoparticles. *Nature* **556**, 360–365 (2018).
8. Lu, J. et al. Enhanced optical asymmetry in supramolecular chiroplasmonic assemblies with long-range order. *Science* **371**, 1368–1374 (2021).
9. González-Rubio, G. et al. Micelle-directed chiral seeded growth on anisotropic gold nanocrystals. *Science* **368**, 1472–1477 (2020).
10. Duan, Y. et al. Optically active chiral CuO "nanoflowers. *J. Am. Chem. Soc.* **136**, 7193–7196 (2014).
11. Yeom, J. et al. Chiromagnetic nanoparticles and gels. *Science* **359**, 309–314 (2018).
12. Ben-Moshe, A. et al. Enantioselective control of lattice and shape chirality in inorganic nanostructures using chiral biomolecules. *Nat. Commun.* **5**, 4302 (2014).
13. Wang, P., Yu, S., Govorov, A. O. & Ouyang, M. Cooperative expression of atomic chirality in inorganic nanostructures. *Nat. Commun.* **8**, 14312 (2017).
14. Kumar, P. et al. Photonically active bowtie nanoassemblies with chirality continuum. *Nature* **615**, 418–424 (2023).
15. Jiang, W. et al. Emergence of complexity in hierarchically organized chiral particles. *Science* **368**, 642–648 (2020).
16. Xu, L. et al. Enantiomer-dependent immunological response to chiral nanoparticles. *Nature* **601**, 366–373 (2022).

17. Kim, H. et al. Gamma-glutamylcysteine- and cysteinylglycine-directed growth of chiral gold nanoparticles and their crystallographic analysis. *Angew. Chem. Int. Ed.* **59**, 12976–12983 (2020).
18. Kumar, J. et al. Detection of amyloid fibrils in Parkinson's disease using plasmonic chirality. *Proc. Natl. Acad. Sci. USA.* **115**, 3225–3230 (2018).
19. Liu, J. et al. Recent advances in inorganic chiral nanomaterials. *Adv. Mater.* **33**, 2005506 (2021).
20. Lv, J. et al. Self-assembled inorganic chiral superstructures. *Nat. Rev. Chem.* **6**, 125–145 (2022).
21. Wu, F. et al. Surface topographical engineering of chiral Au nanocrystals with chiral hot spots for plasmon-enhanced chiral discrimination. *Nano Lett.* **23**, 8233–8240 (2023).
22. Zheng, J. et al. Halide-assisted differential growth of chiral nanoparticles with threefold rotational symmetry. *Nat. Commun.* **14**, 3783 (2023).
23. Cai, J. et al. Polarization-sensitive optoionic membranes from chiral plasmonic nanoparticles. *Nat. Nanotechnol.* **17**, 408–416 (2022).
24. Namgung, S. D. et al. Circularly polarized light-sensitive, hot electron transistor with chiral plasmonic nanoparticles. *Nat. Commun.* **13**, 5081 (2022).
25. Yang, P. et al. Chiral nanostructured bimetallic Au-Ag films for enantiomeric discrimination. *Adv. Mater. Interfaces* **9**, 2200369 (2022).
26. Guan, Y. et al. Chiral plasmonic metamaterials with tunable chirality. *ACS Appl. Mater. Interfaces* **12**, 50192–50202 (2020).
27. Lee, H. E. et al. Cysteine-encoded chirality evolution in plasmonic rhombic dodecahedral gold nanoparticles. *Nat. Commun.* **11**, 263 (2020).
28. Chen, J. et al. Bottom-up synthesis of helical plasmonic nanorods and their application in generating circularly polarized luminescence. *ACS Nano* **15**, 15114–15122 (2021).
29. Bainova, P. et al. Plasmon-assisted chemistry using chiral gold helicoids: toward asymmetric organic catalysis. *ACS Catal.* **13**, 12859–12867 (2023).
30. Hao, C. et al. Unusual circularly polarized photocatalytic activity in nanogapped gold–silver chiroplasmonic nanostructures. *Adv. Funct. Mater.* **25**, 5816–5822 (2015).
31. Wei, X. et al. Enantioselective photoinduced cyclodimerization of a prochiral anthracene derivative adsorbed on helical metal nanostructures. *Nat. Chem.* **12**, 551–559 (2020).
32. Jeong, H. H. et al. Dispersion and shape engineered plasmonic nanosensors. *Nat. Commun.* **7**, 11331 (2016).
33. Solomon, M. L. et al. Nanophotonic platforms for chiral sensing and separation. *Acc. Chem. Res.* **53**, 588–598 (2020).
34. Wang, W. et al. The development of chiral nanoparticles to target NK cells and $CD8^+$ T cells for cancer immunotherapy. *Adv. Mater.* **34**, 2109354 (2022).
35. Hou, K. et al. Chiral gold nanoparticles enantioselectively rescue memory deficits in a mouse model of Alzheimer's disease. *Nat. Commun.* **11**, 4790 (2020).
36. Shukla, N. & Gellman, A. J. Chiral metal surfaces for enantioselective processes. *Nat. Mater.* **19**, 939–945 (2020).
37. Cho, N. H. et al. Cysteine induced chiral morphology in palladium nanoparticle. *Part. Part. Syst. Charact.* **36**, 1900062 (2019).
38. Ni, B., Zhou, J., Stolz, L. & Cölfen, H. A facile and rational method to tailor the symmetry of Au@Ag nanoparticles. *Adv. Mater.* **35**, 2209810 (2023).
39. Deng, G. et al. From symmetry breaking to unraveling the origin of the chirality of ligated $Au_{13}Cu_2$ nanoclusters. *Angew. Chem. Int. Ed.* **57**, 3421–3425 (2018).
40. Ni, B. et al. Chiral seeded growth of gold nanorods into fourfold twisted nanoparticles with plasmonic optical activity. *Adv. Mater.* **35**, 2208299 (2023).
41. Zhang, L. et al. Chiral gold nanorods with five-fold rotational symmetry and orientation-dependent chiroptical properties of their monomers and dimers. *Angew. Chem. Int. Ed.* **62**, e202312615 (2023).
42. Kim, J.-Y. et al. Assembly of gold nanoparticles into chiral superstructures driven by circularly polarized light. *J. Am. Chem. Soc.* **141**, 11739–11744 (2019).
43. Lee, S. et al. Unraveling the chirality transfer from circularly polarized light to single plasmonic nanoparticles. *Angew. Chem. Int. Ed.* **63**, e202319920 (2024).
44. Kim, J. W. et al. Magnetic control of the plasmonic chirality in gold helicoids. *Nano Lett.* **22**, 8181–8188 (2022).
45. Kim, R. M. et al. Enantioselective sensing by collective circular dichroism. *Nature* **612**, 470–476 (2022).
46. Lv, X. et al. Engineering the intrinsic chirality of plasmonic Au@Pd metamaterials for highly sensitive chiroplasmonic hydrogen sensing. *Adv. Mater.* **35**, 2305429 (2023).
47. Wu, F. et al. Synthesis of chiral Au nanocrystals with precise homochiral facets for enantioselective surface chemistry. *Nano Lett.* **22**, 2915–2922 (2022).
48. Li, Z., Jin, J., Yang, F., Song, N. & Yin, Y. Coupling magnetic and plasmonic anisotropy in hybrid nanorods for mechanochromic responses. *Nat. Commun.* **11**, 2883 (2020).
49. Gao, C., Lu, Z. & Yin, Y. Gram-scale synthesis of silica nanotubes with controlled aspect ratios by templating of nickel-hydrazine complex nanorods. *Langmuir* **27**, 12201–12208 (2011).
50. Gao, C., Zhang, Q., Lu, Z. & Yin, Y. Templated synthesis of metal nanorods in silica nanotubes. *J. Am. Chem. Soc.* **133**, 19706–19709 (2011).
51. Lombardi, A. et al. Optical response of individual Au-Ag@SiO_2 heterodimers. *ACS Nano* **7**, 2522–2531 (2013).
52. Lee, J., Park, J. C. & Song, H. A nanoreactor framework of a Au@SiO_2 yolk/shell structure for catalytic reduction of p-nitrophenol. *Adv. Mater.* **20**, 1523–1528 (2008).
53. Liu, Y., Goebl, J. & Yin, Y. Templated synthesis of nanostructured materials. *Chem. Soc. Rev.* **42**, 2610–2653 (2013).
54. Swisher, J. H., Jibril, L., Petrosko, S. H. & Mirkin, C. A. Nanoreactors for particle synthesis. *Nat. Rev. Mater.* **7**, 428–448 (2022).
55. Deng, T.-S. et al. Oxidative etching and metal overgrowth of gold nanorods within mesoporous silica shells. *Chem. Mater.* **27**, 7196–7203 (2015).
56. Thapa, D. K. & Pandey, A. Cloning nanocrystal morphology with soft templates. *Chem. Phys. Lett.* **658**, 315–318 (2016).
57. Van Gordon, K. et al. Single crystal and pentatwinned gold nanorods result in chiral nanocrystals with reverse handedness. *Angew. Chem. Int. Ed.* **63**, e202403116 (2024).
58. Ming, T. et al. Strong polarization dependence of plasmon-enhanced fluorescence on single gold nanorods. *Nano Lett.* **9**, 3896–3903 (2009).
59. Hanske, C., Sanz-Ortiz, M. N. & Liz-Marzan, L. M. Silica-coated plasmonic metal nanoparticles in action. *Adv. Mater.* **30**, 1707003 (2018).
60. Szychowski, B., Leng, H., Pelton, M. & Daniel, M.-C. Controlled etching and tapering of Au nanorods using cysteamine. *Nanoscale* **10**, 16830–16838 (2018).
61. Rodríguez-Fernández, J. et al. The effect of silica coating on the optical response of sub-micrometer gold spheres. *J. Phys. Chem. C* **111**, 13361–13366 (2007).
62. Lu, Y., Yin, Y., Li, Z.-Y. & Xia, Y. Synthesis and self-assembly of Au@SiO_2 core-shell colloids. *Nano Lett.* **2**, 785–788 (2002).
63. Ge, M., Pan, Y., Liu, X., Zhao, Z. & Su, D. Automatic center identification of electron diffraction with multi-scale transformer networks. *Ultramicroscopy* **259**, 113926 (2024).

64. Mao, P. et al. Disorder-induced material-insensitive optical response in plasmonic nanostructures: vibrant structural colors from noble metals. *Adv. Mater.* **33**, 2007623 (2021).
65. Chen, J. et al. Space-confined seeded growth of black silver nanostructures for solar steam generation. *Nano Lett.* **19**, 400–407 (2019).
66. Chen, J. et al. Space-confined seeded growth of Cu nanorods with strong surface plasmon resonance for photothermal actuation. *Angew. Chem. Int. Ed.* **58**, 9275–9281 (2019).
67. Hao, Y. et al. Anticorrosion mechanism of epoxy coating containing mesoporous resorcinol-formaldehyde hollow nanosphere loaded with 8-Hydroxyquinolin. *Appl. Surf. Sci.* **677**, 161014 (2024).
68. Xia, Y., Xiong, Y., Lim, B. & Skrabalak, S. E. Shape-controlled synthesis of metal nanocrystals: simple chemistry meets complex physics? *Angew. Chem. Int. Ed.* **48**, 60–103 (2009).
69. Murshid, N. & Kitaev, V. Role of poly(vinylpyrrolidone) (PVP) and other sterically protecting polymers in selective stabilization of {111} and {100} facets in pentagonally twinned silver nanoparticles. *Chem. Commun.* **50**, 1247–1249 (2014).
70. Chen, Z., Chang, J. W., Balasanthiran, C., Milner, S. T. & Rioux, R. M. Anisotropic growth of silver nanoparticles is kinetically controlled by polyvinylpyrrolidone binding. *J. Am. Chem. Soc.* **141**, 4328–4337 (2019).
71. Liu, X., Li, L., Yang, Y., Yin, Y. & Gao, C. One-step growth of triangular silver nanoplates with predictable sizes on a large scale. *Nanoscale* **6**, 4513–4516 (2014).
72. Zeng, J. et al. Controlling the shapes of silver nanocrystals with different capping agents. *J. Am. Chem. Soc.* **132**, 8552–8553 (2010).
73. Xiong, Y. Morphological changes in Ag nanocrystals triggered by citrate photoreduction and governed by oxidative etching. *Chem. Commun.* **47**, 1580–1582 (2011).
74. Sun, X. et al. Tunable reversal of circular dichroism in the seed-mediated growth of bichiral plasmonic nanoparticles. *ACS Nano* **16**, 19174–19186 (2022).
75. Yang, J. et al. Unraveling the origin of reverse plasmonic circular dichroism from discrete bichiral Au nanoparticles. *Nano Lett.* **24**, 11706–11713 (2024).
76. Zhang, N. N. et al. Synthesis and plasmonic chiroptical properties of double-helical gold nanorod enantiomers. *Adv. Optical Mater.* **11**, 2203119 (2023).
77. Karst, J. et al. Chiral scatterometry on chemically synthesized single plasmonic nanoparticles. *ACS Nano* **13**, 8659–8668 (2019).
78. Cho, N. H. et al. Bioinspired chiral inorganic nanomaterials. *Nat. Rev. Bioeng.* **1**, 88–106 (2023).
79. Abbas, S. U. et al. Chiral metal nanostructures: synthesis, properties and applications. *Rare Met.* **42**, 2489–2515 (2023).
80. Zhang, H., Jin, M. & Xia, Y. Enhancing the catalytic and electrocatalytic properties of Pt-based catalysts by forming bimetallic nanocrystals with Pd. *Chem. Soc. Rev.* **41**, 8035–8049 (2012).
81. Li, S. et al. Emerging trends in chiral inorganic nanomaterials for enantioselective catalysis. *Nat. Commun.* **15**, 3506 (2024).
82. Tan, L., Fu, W., Gao, Q. & Wang, P. P. Chiral plasmonic hybrid nanostructures: a gateway to advanced chiroptical materials. *Adv. Mater.* **36**, 2309033 (2024).
83. Xue, X., Wang, Y. & Han, F. S. A thermoregulated phase-separable chiral Pt nanocatalyst for recyclable asymmetric hydrogenation of alpha-ketoesters. *Chem. Commun.* **53**, 3346–3349 (2017).
84. Yue, X., Xu, L., Lin, H., Xu, C. & Li, S. Construction of Pt/Pt-Au doped chiral nanostructures using arginine and porphyrin assemblies as templates for enantioselective photocatalysis. *Sci. Bull.* **68**, 1764–1771 (2023).
85. Hajji, M. et al. Chiral quantum metamaterial for hypersensitive biomolecule detection. *ACS Nano* **15**, 19905–19916 (2021).
86. Jones, R. R. et al. Chirality conferral enables the observation of hyper-Raman optical activity. *Nat. Photon.* **18**, 982–989 (2024).
87. Meng, D. et al. Interfacial self-assembly of chiral selenide nanomembrane for enantiospecific recognition. *Angew. Chem. Int. Ed.* **62**, e202311416 (2023).
88. Shi, B. et al. Chiral nanoparticles force neural stem cell differentiation to alleviate Alzheimer's disease. *Adv. Sci.* **9**, 2202475 (2022).
89. Qu, A. et al. An NIR-responsive DNA-mediated nanotetrahedron enhances the clearance of senescent cells. *Adv. Mater.* **32**, 2000184 (2020).
90. Xu, Z. et al. Photoinduced elimination of senescent microglia cells in vivo by chiral gold nanoparticles. *Chem. Sci.* **13**, 6642–6654 (2022).
91. Tian, Y. et al. Enantioselective surface-enhanced Raman scattering by chiral Au nanocrystals with finely modulated chiral fields and internal standards. *Adv. Mater.* **36**, 2403373 (2024).
92. Skvortsova, A. et al. Enantioselective molecular detection by surface enhanced Raman scattering at chiral gold helicoids on grating surfaces. *ACS Appl. Mater. Interfaces* **16**, 48526–48535 (2024).
93. Ha, I. H. et al. Synthesis of chiral Ag, Pd, and Pt helicoids inside chiral silica mold. *J. Am. Chem. Soc.* **146**, 30741–30747 (2024).
94. Wan, J. et al. Cu^{2+}-dominated chirality transfer from chiral molecules to concave chiral Au nanoparticles. *J. Am. Chem. Soc.* **146**, 10640–10654 (2024).
95. Bevilacqua, F. et al. Additive-free synthesis of (chiral) gold bipyramids from pentatwinned nanorods. *ACS Materials Lett.* **6**, 5163–5169 (2024).
96. Fu, W. et al. Exploring geometric chirality in nanocrystals for boosting solar-to-hydrogen conversion. *Angew. Chem. Int. Ed.* **63**, e202411871 (2024).
97. Niu, W. et al. Selective synthesis of single-crystalline rhombic dodecahedral, octahedral, and cubic gold nanocrystals. *J. Am. Chem. Soc.* **131**, 697–703 (2009).
98. O'Brien, M. N., Jones, M. R., Brown, K. A. & Mirkin, C. A. Universal noble metal nanoparticle seeds realized through iterative reductive growth and oxidative dissolution reactions. *J. Am. Chem. Soc.* **136**, 7603–7606 (2014).
99. Hu, Y., Zhang, Q., Goebl, J., Zhang, T. & Yin, Y. Control over the permeation of silica nanoshells by surface-protected etching with water. *Phys. Chem. Chem. Phys.* **12**, 11836–11842 (2010).

Acknowledgements

This work was supported by National Key R&D Program of China (2022YFE0113000), National Natural Science Foundation of China (No. 22374144, 22072144, and 22102171), Natural Science Foundation of Jilin Province (No. YDZJ202201ZYTS341), and Department of Science and Technology of Jilin Province (No. 20230505016ZP).

Author contributions

W.N., X.Luan., and L.C. conceived the idea and designed this work. X.Luan. carried out the experiments. Y.T. performed the theoretical calculations. Y.T., F.W., X.Lv., H.W., X.W., F.L., and G.X. participated in the instructions and the discussions of experiments. M.T. carried out the electron tomography reconstructions. W.N. supervised the research. X.Luan, and W.N. co-wrote the manuscript. All authors discussed the results and commented on the manuscript.

Competing interests

The authors declare no competing interests.

Additional information

Supplementary information The online version contains supplementary material available at https://doi.org/10.1038/s41467-025-57624-w.

Correspondence and requests for materials should be addressed to Wenxin Niu.

Peer review information *Nature Communications* thanks the anonymous reviewer for their contribution to the peer review of this work. A peer review file is available.

Reprints and permissions information is available at http://www.nature.com/reprints

Publisher's note Springer Nature remains neutral with regard to jurisdictional claims in published maps and institutional affiliations.

Open Access This article is licensed under a Creative Commons Attribution-NonCommercial-NoDerivatives 4.0 International License, which permits any non-commercial use, sharing, distribution and reproduction in any medium or format, as long as you give appropriate credit to the original author(s) and the source, provide a link to the Creative Commons licence, and indicate if you modified the licensed material. You do not have permission under this licence to share adapted material derived from this article or parts of it. The images or other third party material in this article are included in the article's Creative Commons licence, unless indicated otherwise in a credit line to the material. If material is not included in the article's Creative Commons licence and your intended use is not permitted by statutory regulation or exceeds the permitted use, you will need to obtain permission directly from the copyright holder. To view a copy of this licence, visit http://creativecommons.org/licenses/by-nc-nd/4.0/.

© The Author(s) 2025